Submitted to

32nd International Conference on High Energy Physics, ICHEP04, August 16, 2004, Beijing

Abstract: **6-0175**

Parallel Session **6**

www-h1.desy.de/h1/www/publications/conf/conf_list.html

Measurement of the Inclusive Cross Section for Diffractive Deep Inelastic Scattering at High Q^2

H1 Collaboration

Abstract

A measurement is presented of inclusive diffractive deep inelastic scattering extending to the largest Q^2 values accessed to date. Data taken by the H1 experiment amounting to an integrated luminosity of 63 pb^{-1} are used to investigate the process $ep \to eXY$ in the kinematic range where diffractive exchanges are known to dominate. The Y system is a proton or proton remnant with $M_Y < 1.6$ GeV and $|t| < 1.0$ GeV^2 and it is separated from the X system by a large gap in pseudorapidity. The diffractive reduced cross-section $\sigma_r^{D(3)}(\beta, Q^2, x_{I\!P})$ is extracted in the kinematic range $200 \le Q^2 \le 1600$ $\mathrm{GeV}^2, 0.1 \le (\beta = x/x_{I\!P}) \le 0.9$ and $0.0036 < x_{I\!P} \le 0.05$. The data are used together with other recent measurements at lower Q^2 to test various factorisation properties and models of diffractive DIS. Good agreement is found with predictions based on diffractive parton densities obtained from an NLO QCD fit to lower Q^2 data, evolved using the DGLAP equations, and with a model based on soft colour interactions.

1 Introduction

In Diffractive Deep-Inelastic Scattering (DDIS), it is possible to investigate the parton dynamics of diffractive exchanges with a hard scale provided by the virtuality Q^2 of the point-like virtual photon. The presence of the diffractive exchange implies that the hadronic final state must consist of two distinct systems separated by a large gap in rapidity, as shown in figure 1. The differential cross-section for the process $ep \rightarrow eXY$ can be written as

$$\frac{\mathrm{d}^3\sigma_{ep\rightarrow eXY}}{\mathrm{d}\beta \mathrm{d}Q^2 \mathrm{d}x_{I\!P}} = \frac{4\pi\alpha_{em}^2}{\beta Q^4}\left(1 - y + \frac{y^2}{2}\right)\sigma_r^{D(3)}(\beta, Q^2, x_{I\!P}) \; . \tag{1}$$

Here, the standard DIS variable definitions are used, namely

$$Q^2 = -q^2 \; ; \qquad y = \frac{P.q}{P.k} \; ; \qquad x = \frac{-q^2}{2P.q} \; , \tag{2}$$

determined by the four-momenta of the photon (q), the proton (P) and the incoming positron (k). The additional diffractive variables are defined as

$$x_{I\!P} = \frac{q.(P - p_Y)}{q.P} \; ; \qquad \beta = \frac{-q^2}{2q.(P - p_Y)} \; ; \qquad t = (P - p_Y)^2 \; , \tag{3}$$

where p_Y is the four-momentum of the Y system. Here, $x_{I\!P}$ corresponds to the fraction of the proton beam energy transferred to the longitudinal momentum of the diffractive exchange, β is the fraction of the exchanged longitudinal momentum carried by the quark coupling to the virtual photon and t is the squared 4-momentum transferred at the proton vertex. The reduced cross-section $\sigma_r^{D(3)}(\beta, Q^2, x_{I\!P})$ is related to the diffractive structure functions $F_2^{D(3)}(\beta, Q^2, x_{I\!P})$ and $F_L^{D(3)}(\beta, Q^2, x_{I\!P})$ by

$$\sigma_r^{D(3)} = F_2^{D(3)} - \frac{y^2}{1 + (1-y)^2} F_L^{D(3)} \; , \tag{4}$$

such that $\sigma_r^D \sim F_2^D$ except at very large values of y. In the analysis presented here, neither the squared four-momentum transfer between the virtual photon and the proton, t, nor the mass M_Y are well measured as the Y system is not detected. The measured cross-section is corrected to the region

$$M_Y < 1.6 \text{ GeV} \; ; \qquad |\mathrm{t}| < 1.0 \text{ GeV}^2 \; . \tag{5}$$

The preliminary results presented here are based on high Q^2 data collected with the H1 detector [1] in e^+p interactions at $\sqrt{s} = (k + P) = 319$ GeV at HERA in 1999 and 2000. The data correspond to an integrated luminosity of 63 pb^{-1}. Together with two other preliminary analyses at intermediate [2] and low [3] Q^2, they complete the H1 coverage of the accessible kinematic range as shown in figure 2.

An NLO QCD fit [4] has been made to the intermediate Q^2 data, together with a previous high Q^2 measurement based on a smaller data set (36 pb^{-1} [5]). This fit was based on the hard scattering QCD factorisation theorem for diffraction [6], which implies that diffractive parton densities can be defined for DDIS, such that at fixed $x_{I\!P}$ and t, the Q^2 and β evolution is

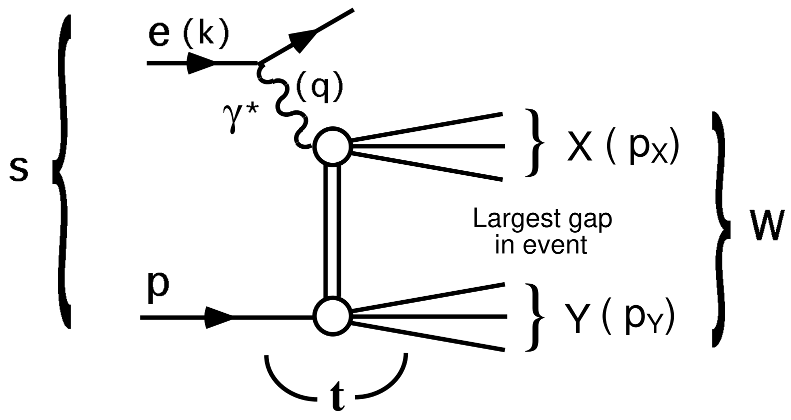

Figure 1: A schematic illustration of the generic DDIS process at HERA, $ep \rightarrow eXY$ (four-momenta are shown in brackets). The positron couples to a virtual photon which interacts with the proton via a colour-singlet exchange, producing two distinct final state systems, X and Y. These two systems are separated by a large gap in rapidity if their masses are small compared with that of the full hadronic final state (W).

described by the DGLAP equations. In the fit, it was also necessary to assume 'Regge factorisation', whereby the diffractive parton densities do not change in shape as $x_{I\!P}$ and t vary and their change in normalisation is given by a parameterisation based on Reggeon flux factors. Both a leading 'pomeron' contribution and a sub-leading 'reggeon' component are included in the fit, with different flux factors and separately evolving parton densities.

The previous measurements have shown no deviation from the diffractive QCD hard scattering factorisation theorem. The Regge factorisation assumption also gives a good approximation to the data, though the low Q^2 data gave an indication that the $x_{I\!P}$ dependence becomes stronger as Q^2 increases [3]. The extended range in Q^2 and precision of the data presented here allow tests of the QCD hard scattering factorisation theorem and Regge factorisation assumption to be made, by comparing the predictions of the NLO QCD fit, evolved using the DGLAP equations, with the new data.

2 Experimental Method

2.1 Selection Criteria and Kinematic Reconstruction

The data used for the analysis are a subset of the high Q^2 inclusive neutral current DIS sample studied in [7]. The diffractive selection requires a large gap in the pseudorapidity distribution of the final state hadrons in the outgoing proton direction, signalling a colour singlet exchange between the photon and the proton to produce two well separated systems X (contained in the main detector) and Y (escaping unobserved into the beampipe). The selection is based on an absence of activity in the components of the H1 detector which are sensitive to energy flow in the proton fragmentation region [2].

The inclusive DIS kinematic variables are obtained from

$$y = y_e^2 + y_{da}(1 - y_{da}) \, ; \qquad Q^2 = \frac{4E_e^2(1-y)}{\tan^2\frac{\theta_e}{2}} \, ; \qquad x = \frac{Q^2}{sy} \, , \tag{6}$$

where y_e is the inelasticity determined by the electron method and y_{da} by the double-angle method [4, 8], E_e is the positron beam energy and θ_e the polar angle of the scattered positron.

The reconstruction of the final state system X uses an algorithm which optimally combines tracking and calorimetric information without double counting [9]. The mass of the X system is reconstructed as

$$M_X^2 = (E^2 - p_x^2 - p_y^2 - p_z^2)_{hadrons} \cdot \frac{y}{y_h} \cdot \delta(M_X^{rec}) \, . \tag{7}$$

Here, $(E, p_x, p_y, p_z)_{hadrons}$ is the 4-vector of the overall hadronic final state observed in the detector, y and y_h are obtained from equation (6) and from the hadron only method, respectively, and $\delta(M_X^{rec})$ corrects for the under-reconstruction of M_X^2 due to losses in the backward direction. This correction is estimated from the simulation. At high M_X ($\gtrsim$ 20 GeV), $\delta(M_X^{rec})$ is approximately equal to 1.07, increasing at lower values of M_X. The diffractive kinematic variables are then reconstructed as

$$\beta = \frac{Q^2}{Q^2 + M_X^2} \, ; \qquad x_{I\!P} = \frac{x}{\beta} \, . \tag{8}$$

2.2 Corrections to the Data

The RAPGAP [10] Monte Carlo generator is designed to describe the DDIS process $ep \rightarrow eXp$. It is used to correct the data for the effects of the detector acceptance and kinematic migrations due to the finite detector resolution and imperfections in the reconstruction. RAPGAP uses diffractive parton densities extracted from a LO QCD fit, similar to that described in section 1, but performed on earlier H1 data [8]. The parton densities are convoluted with QCD matrix elements up to order α_s. Further QCD radiation is simulated via an interface to the ARIADNE [11] program, which is an implementation of the Colour Dipole Model [11, 12]. As required by the data [8], a sub-leading exchange is also included, with parton densities obtained from a parameterisation for the π-meson [13]. QED radiation is simulated via an interface to the HERACLES [14] program.

The factor 1.08 ± 0.10 required to correct the data to the measured range $M_Y < 1.6$ GeV, $|t| < 1$ GeV^2 was evaluated using the DIFFVM [15] generator, which simulates diffractive events both with intact final state protons and with proton dissociation. Migrations into the measured range from very large $x_{I\!P} > 0.15$ or large $M_Y > 5$ GeV values are estimated using the DJANGO [16] generator of non-diffractive DIS. This program is an interface between the HERACLES ep event generator and the ARIADNE program.

Corrections are made for several small background contributions to the data. The contamination from hard diffractive photoproduction processes, in which a particle from the hadronic final state fakes the signature of the scattered electron, is estimated from the number of events in the data in which the positron candidate has negative instead of positive charge. The background is statistically removed from the event sample under the assumption that it is charge-symmetric. More details can be found in [7]. The QED-Compton ($ep \to ep\gamma$) background is subtracted using the predictions of the COMPTON [17] Monte Carlo generator. The background from photon photon events ($ep \to epe^+e^-$), where two photons radiated from the incoming electron and proton interact to produce a lepton pair, is subtracted using the LPAIR [18] generator.

Comparisons of the full simulation with the uncorrected data for several kinematic distributions can be seen in figure 3. The simulation gives a good description of the data for all variables.

2.3 Extraction of the Reduced Cross-Section

After corrections for backgrounds, detector acceptance and migrations and QED radiation, the diffractive reduced cross section is extracted from the measured differential cross section using equation 1. Two different binning schemes are used, in order to extract data at fixed Q^2, β and x (sections 3.1 and 3.3) and at fixed Q^2, β and $x_{I\!P}$ (section 3.2). The data are quoted at the centre of each analysis bin after applying corrections for the cross section variation across the bin, calculated analytically using the results of the QCD fit in [8]. The acceptance, purity and stability[1] for each quoted bin is required to be greater than 30 %.

A full analysis of the systematic uncertainties of the measurement was performed. The sources of systematic uncertainty associated with the reconstruction of the scattered electron and the final state hadrons are discussed in [7]. Those uncertainties particular to the diffractive measurement are described in [2]. The dominant systematic uncertainties arise from the corections for smearing about the $M_{\rm Y}$ boundary of the measurement, the subtraction of noise in the hadronic final state reconstruction and, at high $x_{I\!P}$, the correction for smearing into the sample from very large $x_{I\!P}$ as described using the DJANGO model. The systematic error on the final cross-sections is approximately 15% on average, comparable to the statistical error.

3 Results

3.1 The $x_{I\!P}$ Dependence of σ_r^D

Figure 4 shows the $x_{I\!P}$ dependence of the data at fixed β and Q^2 compared with the previous H1 high Q^2 data [5]. The new measurement extends the kinematic range in β and Q^2. In the region of overlap of the two measurements there is good agreement. The prediction based on the NLO QCD fit to lower Q^2 data yields a good description after DGLAP evolution of the parton densities. A possible exception is the highest β region, where the fit tends to overshoot the data. Also shown separately is the Pomeron component of the fit, which dominates the prediction at large β, but is clearly insufficient at low β and high $x_{I\!P}$. When the sub-leading Reggeon component is also included, the description in the low β region is much better.

[1]The purity (stability) of a bin is defined as the fraction of events reconstructed (generated) in a bin that were also generated (reconstructed) in that bin, according to the simulation.

3.2 The Q^2 and β Dependences of σ_r^D

The Q^2 dependence of $x_{I\!P}\sigma_r^D$ at fixed β and $x_{I\!P}$ is compared with the QCD fit in figures 5 and 6. Also included in these figures are the medium Q^2 data used in the fit and low Q^2 data which were not included in the fit. Over most of the β range, the data display large positive scaling violations, indicative of a strongly gluon-dominated structure. Exact scaling occurs at a fractional momentum of around $\beta \approx 0.65$. The predictions of the NLO QCD fit to lower Q^2 data are in good agreement with the new high Q^2 data. For $x_{I\!P} = 0.01$ (figure 5), the sub-leading reggeon component is negligible. For $x_{I\!P} = 0.03$ (figure 6), the data cannot be described without the admixture of the quark-dominated sub-leading exchange.

$x_{I\!P}\sigma_r^D$ is shown as a function of β at fixed $x_{I\!P}$ and Q^2 in figures 7 and 8. Again, the new data show that the observations from lower Q^2 persist into the new kinematic regime. At relatively low $x_{I\!P} = 0.01$ (figure 7), the data are approximately flat as a function of β. At higher $x_{I\!P} = 0.03$ (figure 8), the data show a tendency to decrease with increasing β. This effect is reproduced by the QCD fit, where it arises due to the evolution of the pomeron parton densities to the higher Q^2 range accessed and the increased contribution from the sub-leading exchange.

Figures 9 and 10 show the same distributions as figures 5-8, but restricted to β and Q^2 values which contain high Q^2 data points, allowing a closer inspection of the level of agreement between the predictions of the NLO QCD fit and the data.

3.3 Comparison with Soft Colour Rearrangement Models

In the Soft Colour Interactions (SCI) model of Edin, Ingelman and Rathsman [19], the underlying hard interaction is the same for both diffractive and non-diffractive events. Soft interactions then take place, in which colour, but not momentum, is transferred between the outgoing partons. The colour strings connecting the outgoing partons are thus rearranged and rapidity gaps can be produced where there is no colour connection between neighbouring partons. The original SCI model contains just one free parameter, which is the probability of the soft colour rearrangements occurring. A modification to this model uses a Generalised Area Law (GAL) [20], whereby configurations with colour strings spanning a large area in energy-momentum space are exponentially suppressed.

Figure 11 shows the $x_{I\!P}$ dependence of the data at fixed β and Q^2, compared with both versions of the SCI model. The original SCI model is able to describe the data in the highest β bin at high $x_{I\!P}$ but undershoots the data almost everywhere else. The model incorporating the generalised area law produces a much better overall description and is able to describe the data well everywhere except at the lowest β.

4 Conclusions

A new measurement of inclusive DDIS at high Q^2 has been presented, which extends the kinematic phase-space compared with previous data and increases the statistical precision. The diffractive reduced cross-section $\sigma_r^{D(3)}(\beta, Q^2, x_{I\!P})$ was extracted from the data in the kinematic range $200 \leq Q^2 \leq 1600~\mathrm{GeV}^2, 0.1 \leq \beta \leq 0.9$ and $0.0036 < x_{I\!P} \leq 0.05$ and found to be consistent with previous H1 measurements. The new data confirm the positive scaling violations persisting to large values of $\beta \sim 0.65$ and the relatively flat β dependence observed in previous analyses. The predictions of an NLO QCD fit to lower Q^2 measurements describe the data well. The data are thus consistent with the diffractive hard scattering factorisation theorem and the Regge factorisation assumption. They can be described by a leading heavily gluon dominated 'Pomeron' exchange, complemented by a non-negligible sub-leading Reggeon contribution at large $x_{I\!P}$ and low β. The SCI model incorporating a generalised area law is found to produce a good description of the data except at the lowest β.

Acknowledgements

We are grateful to the HERA machine group whose outstanding efforts have made this experiment possible. We thank the engineers and technicians for their work in constructing and now maintaining the H1 detector, our funding agencies for financial support, the DESY technical staff for continual assistance and the DESY directorate for support and for the hospitality which they extend to the non-DESY members of the collaboration.

References

[1] H1 Collaboration, I. Abt et al., Nucl. Instr. Meth. A386 (1997) 310 and 348.

[2] H1 Collaboration, *Measurement of the Diffractive Structure Function* $F_2^{D(3)}(\beta, Q^2, x_{I\!P})$ *at HERA*, paper 808 submitted to EPS2001, Budapest, Hungary, July 2001.

[3] H1 Collaboration, *Measurement of the Diffractive Deep-Inelastic Scattering Cross Section at Low* Q^2, paper 981 submitted to ICHEP2002, Amsterdam, Holland, July 2002.

[4] H1 Collaboration, *Measurement and NLO DGLAP QCD Interpretation of Diffractive Deep-Inelastic Scattering at HERA*, paper 980 submitted to ICHEP2002, Amsterdam, Holland, July 2002.

[5] H1 Collaboration, *Measurement and Interpretation of the Diffractive Structure Function* $F_2^{D(3)}$ *at HERA*, Contributed paper no. 571 submitted to ICHEP 1998 (Vancouver).

[6] J. Collins, Phys. Rev. D57 (1998) 3051 and erratum-ibid. D61 (2000) 019902.

[7] H1 Collaboration, C. Adloff et al., Accepted by Eur. Phys. J, 04/03.

[8] H1 Collaboration, C. Adloff et al., Z. Phys. C76 (1997) 613.

[9] H1 Collaboration, C. Adloff et al., Z. Phys. C74 (1997) 221.

[10] H. Jung, Comp. Phys. Commun. 86 (1995) 147.

[11] L. Lonnblad, Comp. Phys. Comm. 71 (1992) 15-31.

[12] G. Gustafson, U. Pettersson,Nucl. Phys. B306 (1988) 746; B. Andersson, G. Gustafson, L. Lonnblad, U. Pettersson, Z. Phys. C43 (1989) 625; B. Andersson, G. Gustafson, L. Lonnblad, Nucl. Phys. B339 (1990) 393-406.

[13] J. Owens, Phys. Rev, D30 (1984) 943.

[14] A. Kwiatkowski, H. Speisberger, H. Möhring, Comp. Phys. Comm. 69 (1992) 155.

[15] B. List, A. Mastroberardino, *DIFFVM: A Monte Carlo Generator for diffractive processes in ep scattering*, in A. Doyle, G. Grindhammer, G. Ingelman, H. Jung (eds.): *Monte Carlo Generators for HERA Physics*, DESY-PROC-1999-02 (1999) 396.

[16] G. Schuler, H. Spiesberger, Proc. of the Workshop on Physics at HERA, Vol. 3, eds. W. Buchmüller, G. Ingelman, Hamburg, DESY (1992) 1419.

[17] A. Courou, P. Kessler, Phys. Rev. D46 (1992) 117.

[18] S. P. Baranov, O. Duenger, H. Shooshtari, J. A. M. Vermaseren, *Hamburg 1991, Proceedings, Physics at HERA, vol. 3* 1478-1482. (see High Energy Physics Index 30 (1992) No. 12988).

[19] A. Edin, G. Ingelman, J. Rathsman, Phys. Lett. B366 (1996) 371-378; A. Edin, G. Ingelman, J. Rathsman, Z. Phys. C75 (1997) 57-70.

[20] J. Rathsman, Phys. Lett. B452 (1999) 364-371.

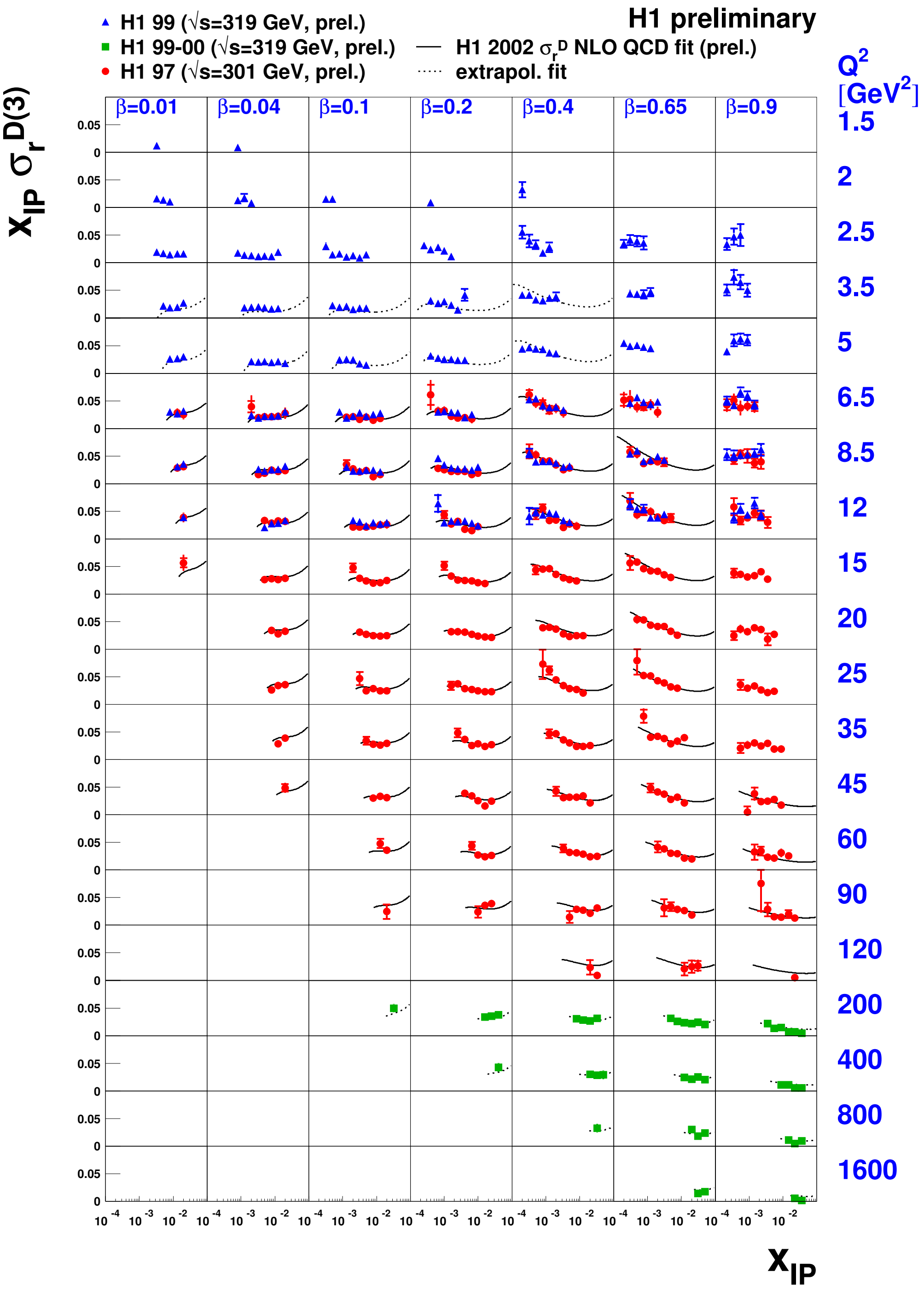

Figure 2: Reduced cross section $\sigma_r^{D(3)}$ from this measurement, compared with recent H1 measurements at lower Q^2. $x_{I\!P}\sigma_r^{D(3)}(x_{I\!P}, \beta, Q^2)$ is shown as a function of $x_{I\!P}$ for fixed β and Q^2. Here and elsewhere, the inner error bars represent statistical errors and the outer error bars correspond to the total error, given by the quadratic sum of statistical and systematic errors. Normalization uncertainties, which are of the order of $6-8\%$ for each data set, are not shown. Also shown is the prediction for $x_{I\!P}\sigma_r^{D(3)}$ for $\sqrt{s} = 319$ GeV from the NLO QCD fit performed to the medium Q^2 data. The fit results are shown as solid lines for the fitted data ($6.5 \le Q^2 \le 120$ GeV^2 and $M_X > 2$ GeV). The extrapolation to low ($Q^2 < 6.5$ GeV^2) and high ($Q^2 > 120$ GeV^2) values of Q^2 is shown as dotted lines.

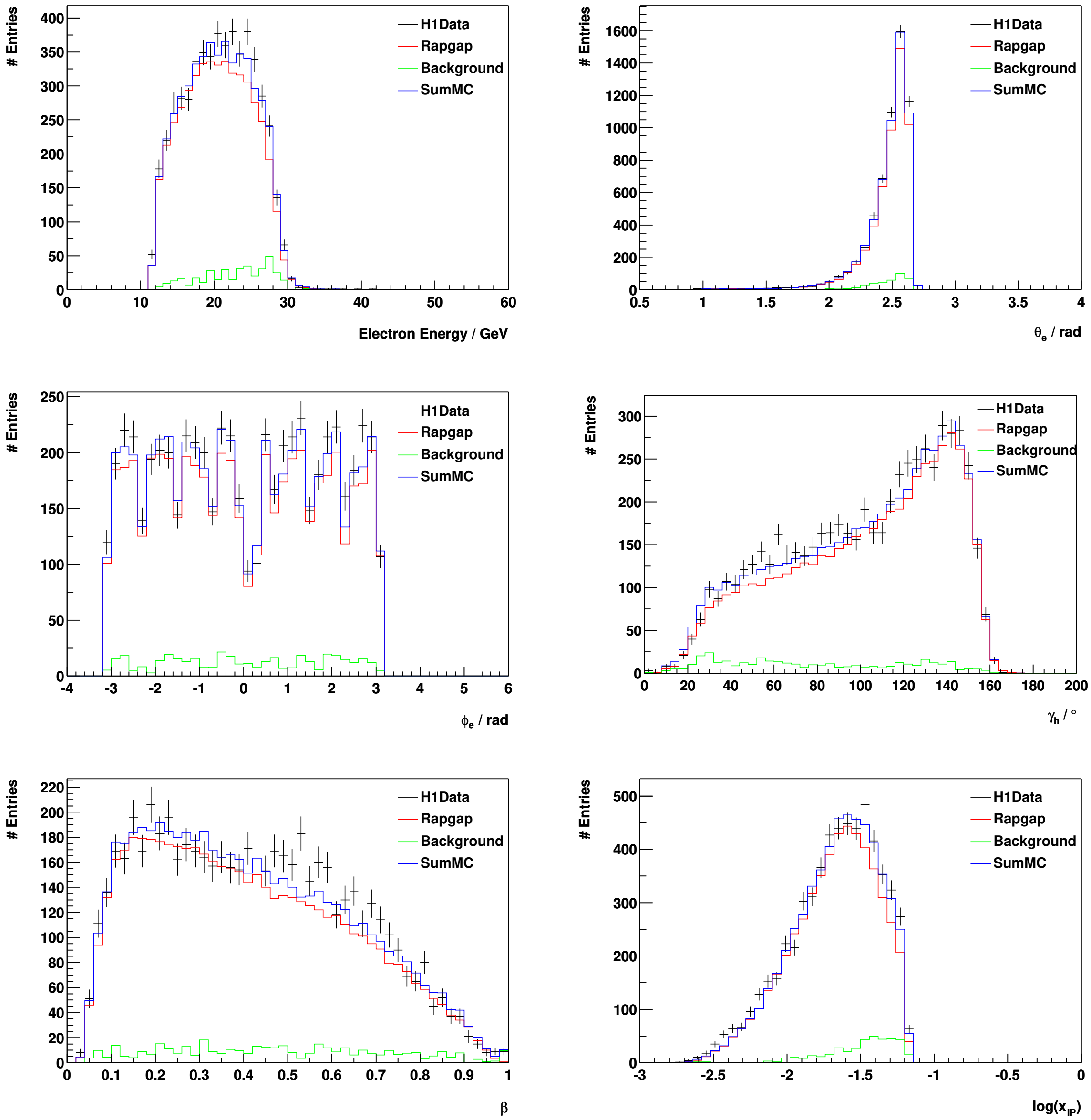

Figure 3: Distributions of the scattered electron energy (top left), the polar (top right) and azimuthal (middle left) angles of the positron, the polar angle of the X system (middle right), the reconstructed β (bottom left) and $\log x_{I\!P}$ (bottom right) of the high Q^2 DDIS event sample. The uncorrected data are compared with the predictions of the RAPGAP simulation, the total background simulation and the sum of both.

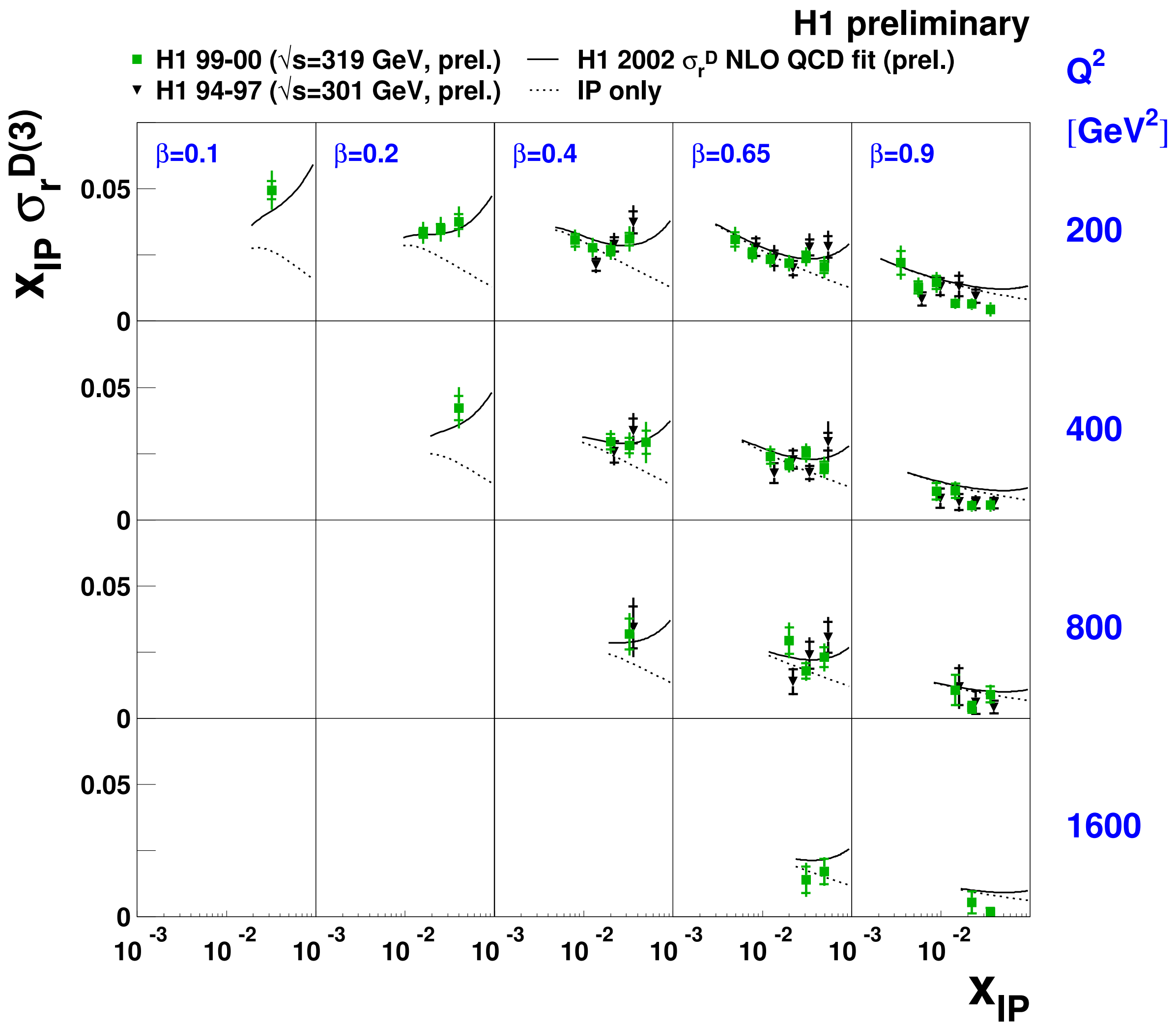

Figure 4: The measured reduced cross section $x_{I\!P}\sigma_r^{D(3)}$, plotted as a function of $x_{I\!P}$ at fixed (β, Q^2) from the present measurement, compared with the previous H1 preliminary measurement based on 1994-1997 data [5]. Also shown is the prediction for $x_{I\!P}\sigma_r^{D(3)}$ for $\sqrt{s} = 319$ GeV from the NLO QCD fit performed to the medium Q^2 data. The solid curves correspond to the sum of "Pomeron" and "Reggeon" exchange contributions in the fit, whereas the dotted curves represent the contribution from "Pomeron" exchange alone.

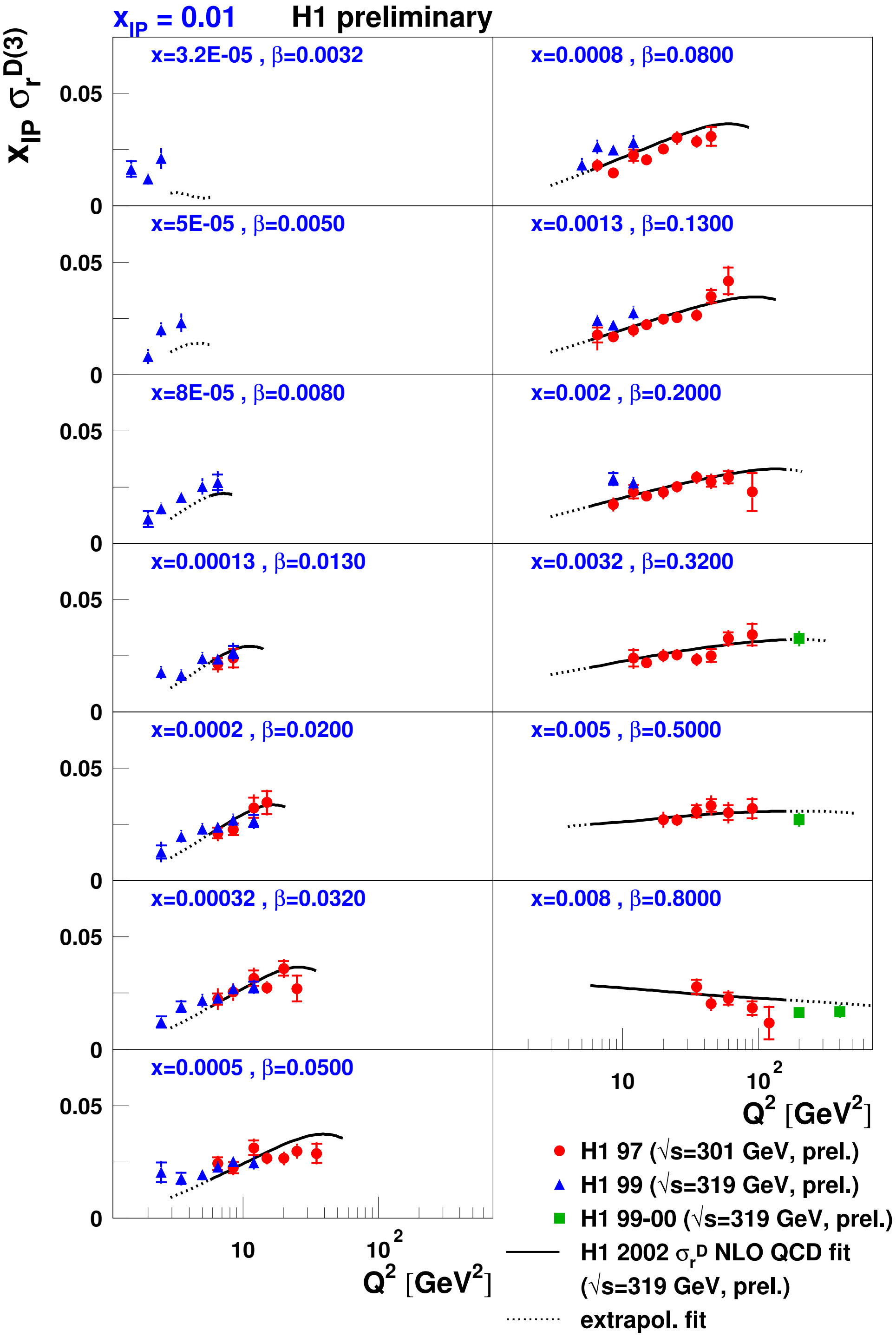

Figure 5: Reduced cross section $\sigma_r^{D(3)}$ from this measurement, compared with two recent H1 measurements at lower Q^2. $x_{I\!P}\sigma_r^{D(3)}(x_{I\!P}, \beta, Q^2)$ is shown as a function of Q^2 at fixed x or β and $x_{I\!P} = 0.01$. Also shown is the prediction for $x_{I\!P}\sigma_r^{D(3)}$ for $\sqrt{s} = 319$ GeV from the NLO QCD fit performed to the medium Q^2 data.

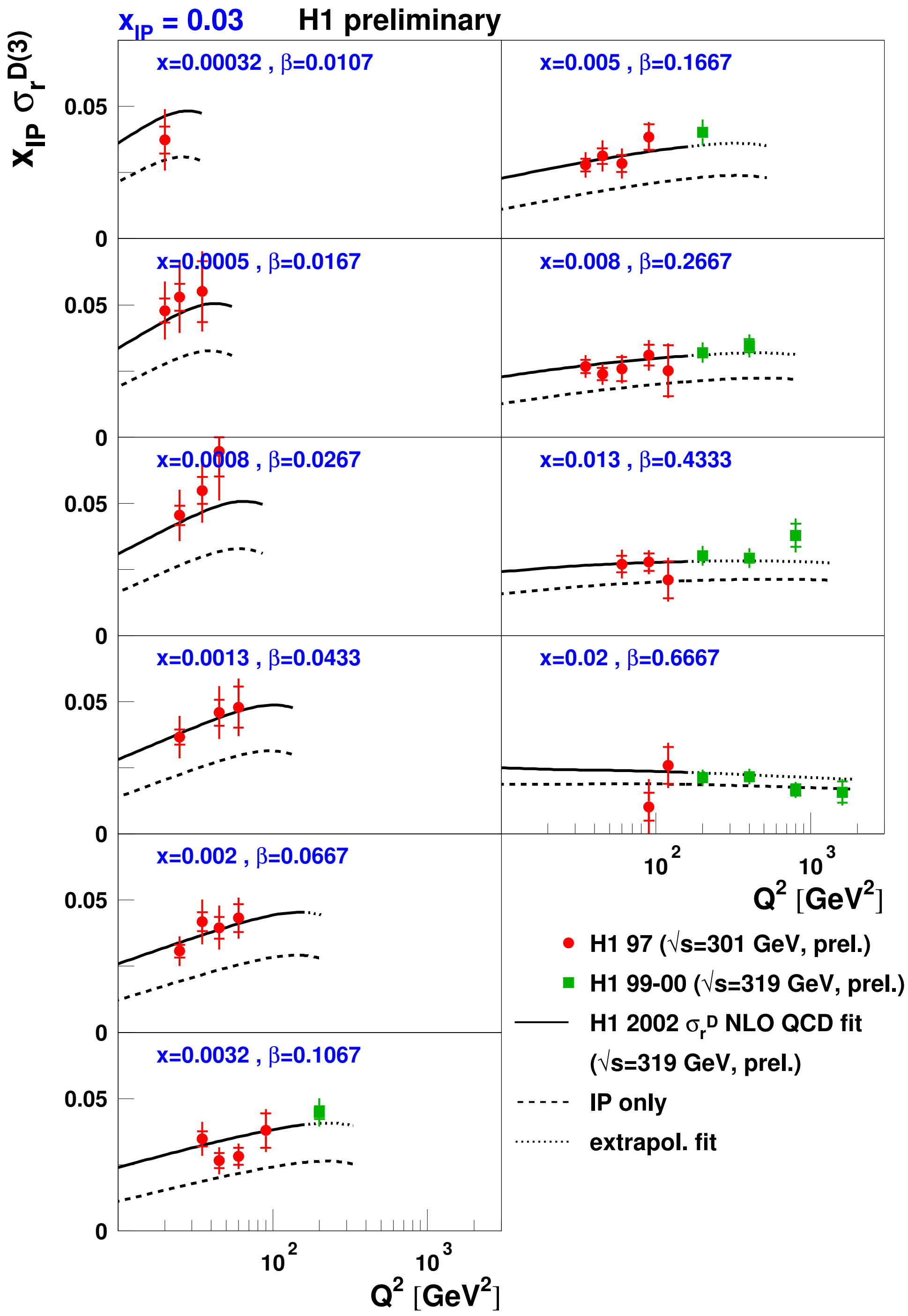

Figure 6: Reduced cross section $\sigma_r^{D(3)}$ from this measurement, compared with a recent H1 measurement at lower Q^2. $x_{I\!P}\sigma_r^{D(3)}(x_{I\!P}, \beta, Q^2)$ is shown as a function of Q^2 at fixed x or β and $x_{I\!P} = 0.03$. Also shown is the prediction for $x_{I\!P}\sigma_r^{D(3)}$ for $\sqrt{s} = 319$ GeV from the NLO QCD fit performed to the medium Q^2 data and the fit prediction for the pomeron contribution alone.

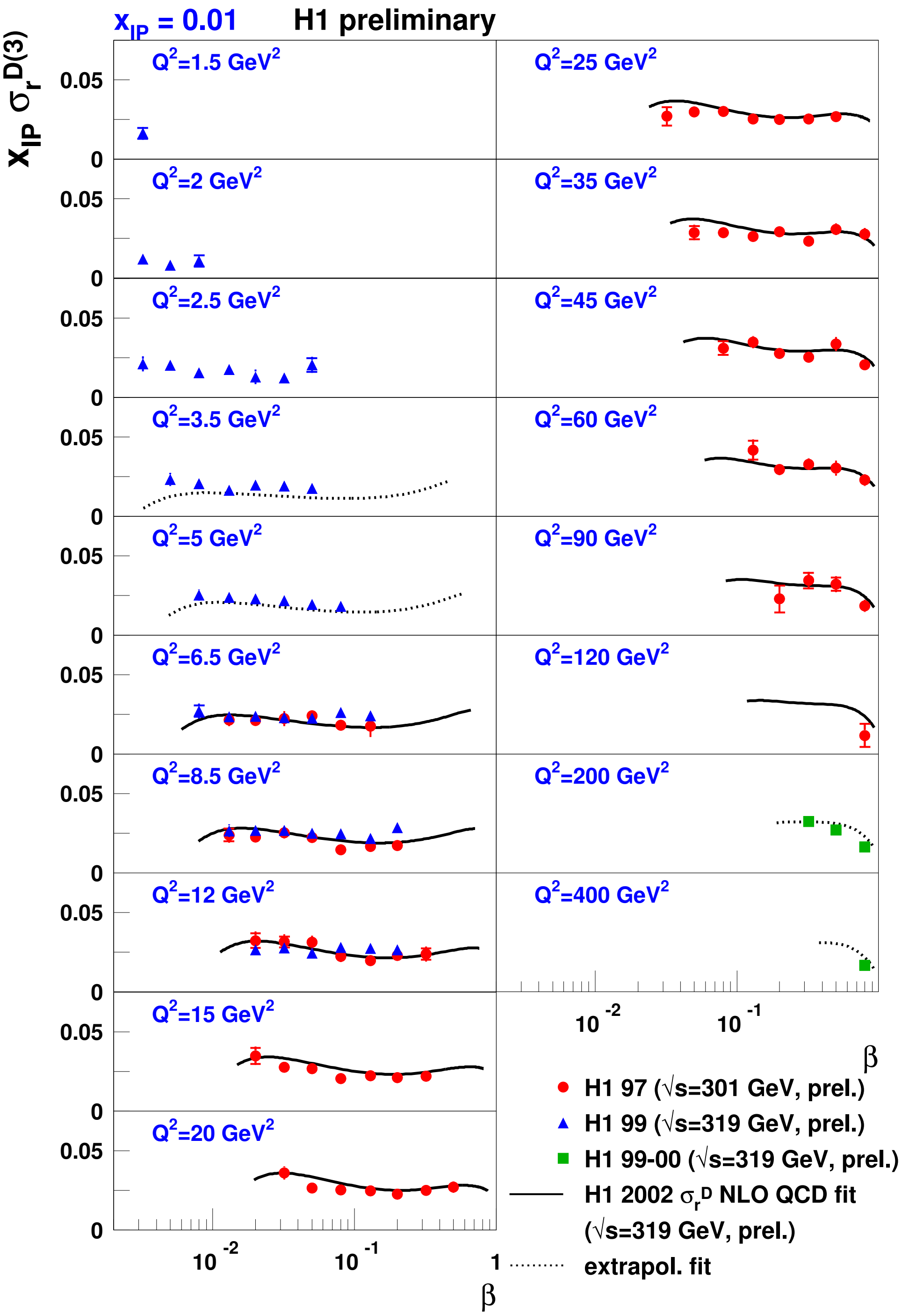

Figure 7: Reduced cross section $\sigma_r^{D(3)}$ from this measurement, compared with two recent H1 measurements at lower Q^2. $x_{I\!P}\sigma_r^{D(3)}(x_{I\!P}, \beta, Q^2)$ is shown as a function of β at fixed Q^2 and $x_{I\!P} = 0.01$. Also shown is the prediction for $x_{I\!P}\sigma_r^{D(3)}$ for $\sqrt{s} = 319$ GeV from the NLO QCD fit performed to the medium Q^2 data.

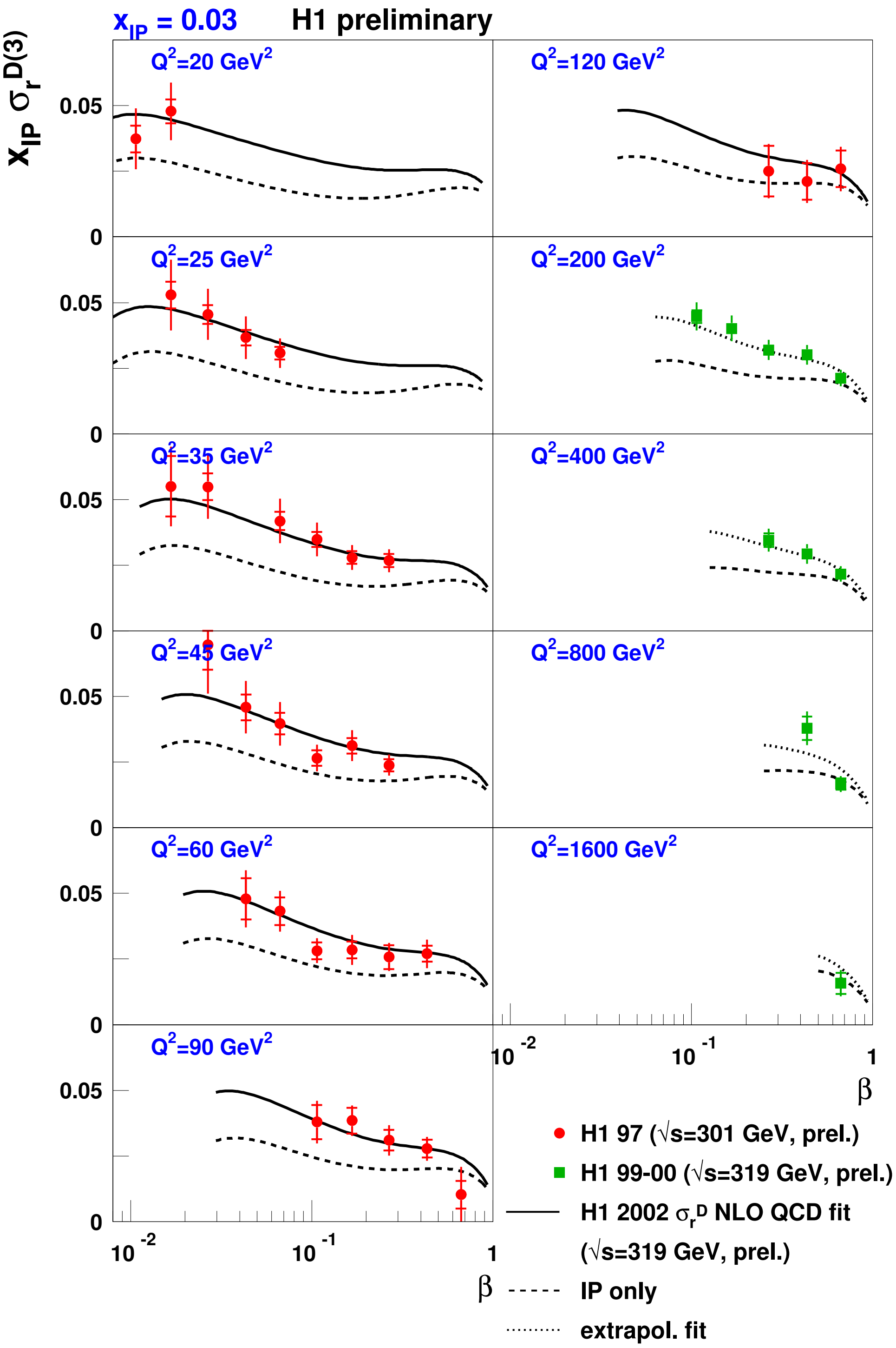

Figure 8: Reduced cross section $\sigma_r^{D(3)}$ from this measurement, compared with a recent H1 measurements at lower Q^2. $x_{I\!P}\sigma_r^{D(3)}(x_{I\!P}, \beta, Q^2)$ is shown as a function of β at fixed Q^2 and $x_{I\!P} = 0.03$. Also shown is the predicion for $x_{I\!P}\sigma_r^{D(3)}$ for $\sqrt{s} = 319$ GeV from the NLO QCD fit performed to the medium Q^2 data and the fit prediction for the pomeron contribution alone.

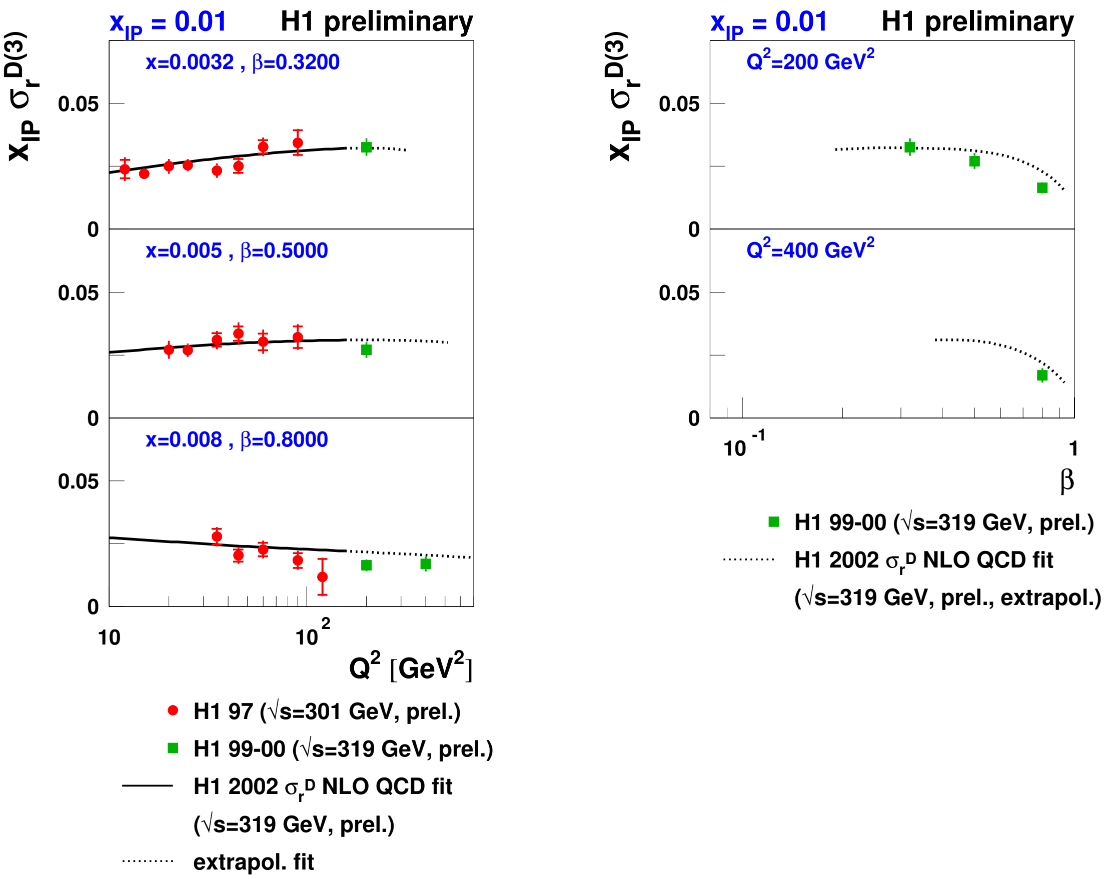

Figure 9: Reduced cross section $\sigma_r^{D(3)}$ at fixed $x_{I\!P} = 0.01$ from this measurement, compared with a recent H1 measurement at lower Q^2. $x_{I\!P}\sigma_r^{D(3)}(x_{I\!P}, \beta, Q^2)$ is shown as a function of Q^2 at fixed x or β (left) and as a function of β at fixed Q^2 (right). Also shown is the predicion for $x_{I\!P}\sigma_r^{D(3)}$ for $\sqrt{s} = 319$ GeV from the NLO QCD fit performed to the medium Q^2 data.

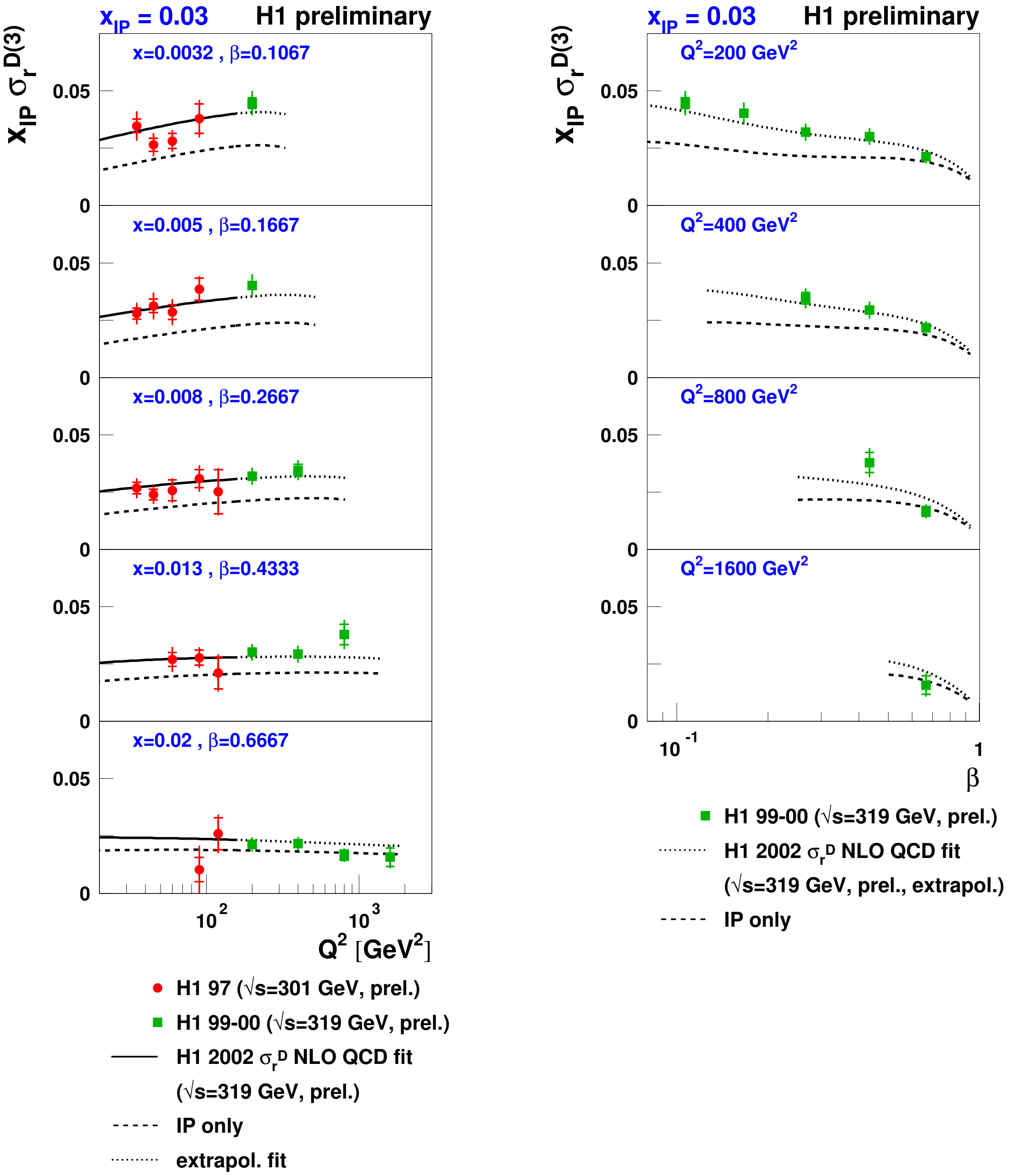

Figure 10: Reduced cross section $\sigma_r^{D(3)}$ at fixed $x_{I\!P} = 0.03$ from this measurement, compared with a recent H1 measurement at lower Q^2. $x_{I\!P}\sigma_r^{D(3)}(x_{I\!P}, \beta, Q^2)$ is shown as a function of Q^2 at fixed x or β (left) and as a function of β at fixed Q^2 (right). Also shown is the predicion for $x_{I\!P}\sigma_r^{D(3)}$ for $\sqrt{s} = 319$ GeV from the NLO QCD fit performed to the medium Q^2 data and the prediction for the pomeron component alone.

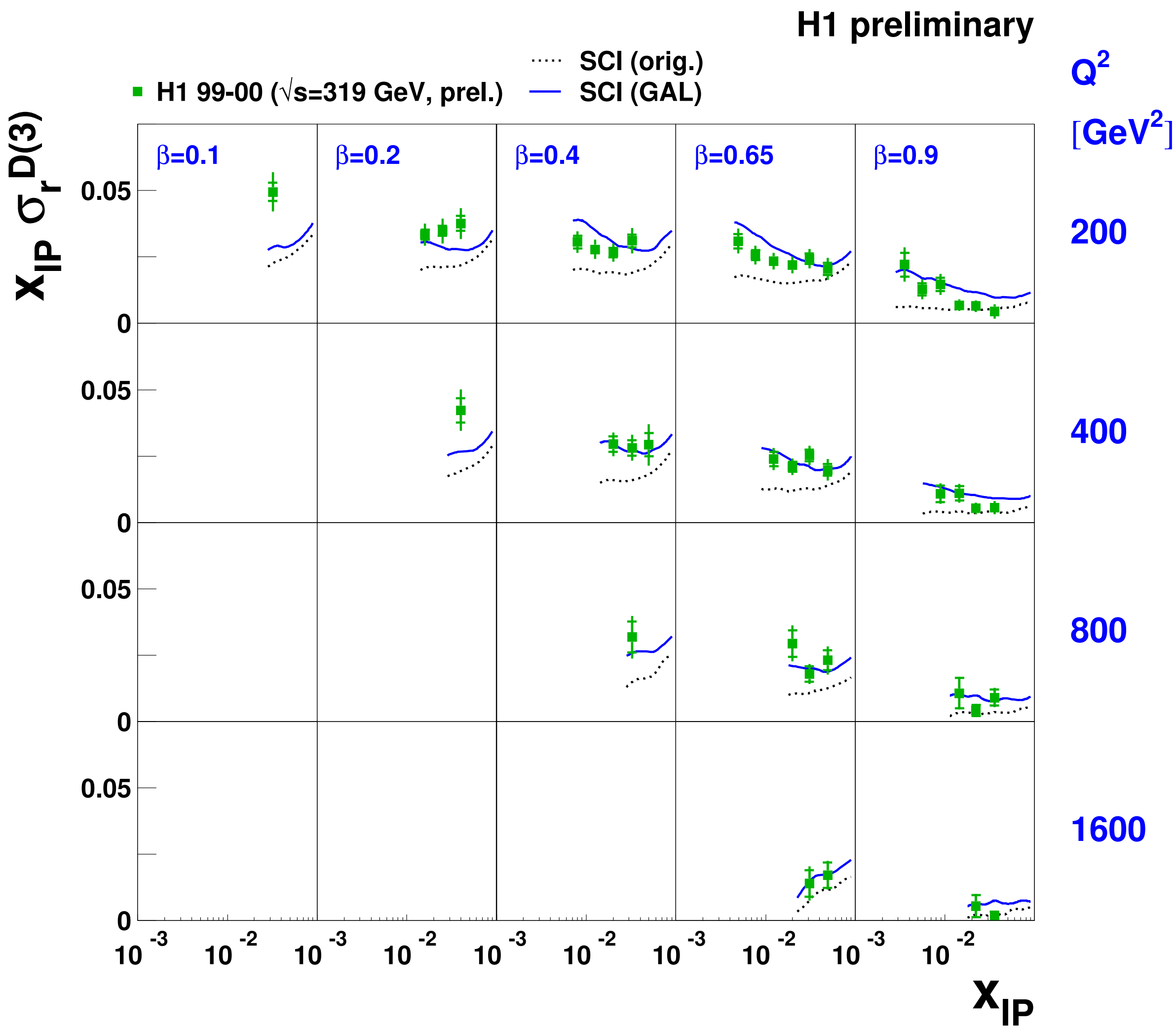

Figure 11: The measured reduced cross section $x_{I\!P}\sigma_r^{D(3)}$, plotted as a function of $x_{I\!P}$ at fixed (β, Q^2) (green data points). The data are compared with the predictions of the original Soft Colour Interactions (SCI) model (dashed curves) and its refinement based on a generalized area law (solid curves), both obtained with the LEPTO 6.5.2β MC generator.